nature geoscience

ARTICLES

https://doi.org/10.1038/s41561-022-00947-w

Check for updates

High water content of arc magmas recorded in cumulates from subduction zone lower crust

B. M. Urann[1,2,3] ✉, V. Le Roux[2], O. Jagoutz[4], O. Müntener[5], M. D. Behn[6] and E. J. Chin[7]

Magmatic volatiles (for example, water) are abundant in arc melts and exert fundamental controls on magma evolution, eruption dynamics and the formation of economic ore deposits. To constrain the H_2O content of arc magmas, most studies have relied on measuring extrusive products and mineral-hosted melt inclusions. However, these methods have inherent limitations that obfuscate the full range of H_2O in arc magmas. Here, we report secondary-ion mass spectrometry measurements of volatile (H_2O, F, P, S, Cl) abundances in lower-crustal cumulate minerals from the Kohistan palaeo-arc (northwestern Pakistan) and determine H_2O abundances of melts from which the cumulates crystallized. Pyroxenes retained magmatic H_2O abundances and record damp (less than 1 wt% H_2O) to hydrous (up to 10 wt% H_2O) primitive melts. Subsequent crystal fractionation led to formation of super-hydrous melts with approximately 12–20 wt% H_2O, predicted petrologically yet virtually absent from the melt-inclusion record. Porphyry copper deposits are probably a natural eventuality of fluid exsolution from super-hydrous melts, corroborating a growing body of evidence.

Subduction is the primary mechanism of fluid transfer from Earth's surface to the mantle and leads to the generation of volatile-rich arc magmas. Volatile contents (for example, H_2O, CO_2, S, F, Cl) of arc magmas influence the dynamics of volcanic eruptions, the nature of volcanic gases and magmatic fluids and the compositional and physical characteristics of arc crust[1]. A major challenge in determining the range of H_2O abundances in arc melts is that H_2O solubility in basaltic melts decreases with decreasing pressure, from >20 wt% H_2O at 1 GPa and 1,200 °C (ref. [2]) to 0.1 wt% at 1 atmosphere. As a result of this strong pressure dependence on volatile solubility, most arc magmas reach volatile saturation and exsolve volatiles during their ascent through arc crust. To circumvent the effects of volatile loss before and during eruption, workers have relied on melt inclusions entrapped in olivine and clinopyroxene (cpx) phenocrysts[3,4]. Melt inclusions have been interpreted to preserve the H_2O content of arc magmas at depth where olivine crystallized[4], yielding a range of 1.30–7.15 wt% H_2O (melt Mg# 39–82; molar Mg/(Mg+Fe)) (ref. [5]). However, subsequent studies have demonstrated that diffusive re-equilibration of hydrogen in melt inclusions is fast (days to hours)[6–8], and therefore melt inclusions may not record the initial H_2O content of arc magmas in the lower arc crust[5,9].

Other approaches to estimate H_2O contents of arc magmas have yielded promising results. Previous workers have shown that arc cumulate minerals may be more reliable than melt inclusions as indicators of magma hydration state at H_2O contents above ~8 wt%. Phase equilibria studies of cumulate amphibole suggest H_2O concentrations up to 10–15 wt% (refs. [10–12]), while plagioclase compositional phase equilibria calculations indicate melts up to 9 wt% H_2O[13]. Similar thermodynamic and experimental approaches at Mount Pinotubo[14], the west-central Mexico volcanic belt[15] and the porphyry copper-rich Gangdese magmatic belt[16] (southern Tibet) have implicated the presence of super-hydrous (>10 wt% H_2O) magmas. Combined approaches of experimental petrology and electrical conductivity have also inferred the presence of super-hydrous magmas with >8 wt% H_2O in andesitic melts beneath the central Andes and Cascades[17]. Results from these studies suggest that arc magmas should contain more H_2O than inferred from melt-inclusion measurements. Reconciling these disparate approaches to quantify arc magma H_2O abundances is critical for evaluating the propensity of copper porphyry formation, which is thought to result from exsolution of hydrous, Cl-rich magmas[18].

In this article, we build on the arc cumulate approach to explore the H_2O content of primitive and evolved arc magmas by in situ geochemical techniques. Lower-crustal cumulates typically crystallize at 20–50 km depth, before H_2O saturation, exsolution and degassing at shallower levels. We present secondary-ion mass spectrometry (SIMS) measurements of volatile abundances (H_2O, F, P, S, Cl) in cumulate minerals (clinopyroxene ± orthopyroxene, garnet, amphibole) from the Kohistan lower arc crust. New volatile-, major- and trace-element data on mineral phases are combined with petrological models and experimentally calibrated partition coefficients[19] to determine the compositional evolution (and, in particular, H_2O abundances) of the silicate melts from which the cumulates crystallized. This approach provides a fruitful avenue to determine the range of H_2O abundances in arc melts from primitive to evolved compositions.

Lower-crustal cumulates from the Kohistan arc terrane

The Cretaceous Kohistan palaeo-arc terrane, exposed in the western part of the Himalaya Mountain range (northwestern Pakistan, Supplementary Fig. 1) is a near-complete section of volcanic, plutonic and upper mantle rocks obducted 50 million years ago (Ma) onto India[20]. The Kohistan lower crust can be differentiated into two domains: the Jijal Complex at the stratigraphic base (1.5–0.8 GPa) and the Chilas Complex, obliquely situated above (0.6–0.7 GPa)

[1]MIT-WHOI Joint Program, Marine Geology and Geophysics, Woods Hole Oceanographic Institution, Woods Hole, MA, USA. [2]Geology and Geophysics Department, Woods Hole Oceanographic Institution, Woods Hole, MA, USA. [3]Department of Geology and Geophysics, University of Wyoming, Laramie, WY, USA. [4]Department of Earth, Atmospheric, and Planetary Sciences, Massachusetts Institute of Technology, Cambridge, MA, USA. [5]Institute of Earth Sciences, University of Lausanne, Lausanne, Switzerland. [6]Department of Earth and Environmental Sciences, Boston College, Chestnut Hill, MA, USA. [7]Geosciences Research Division, Scripps Institution of Oceanography, University of California San Diego, La Jolla, CA, USA. ✉e-mail: burann@uwyo.edu

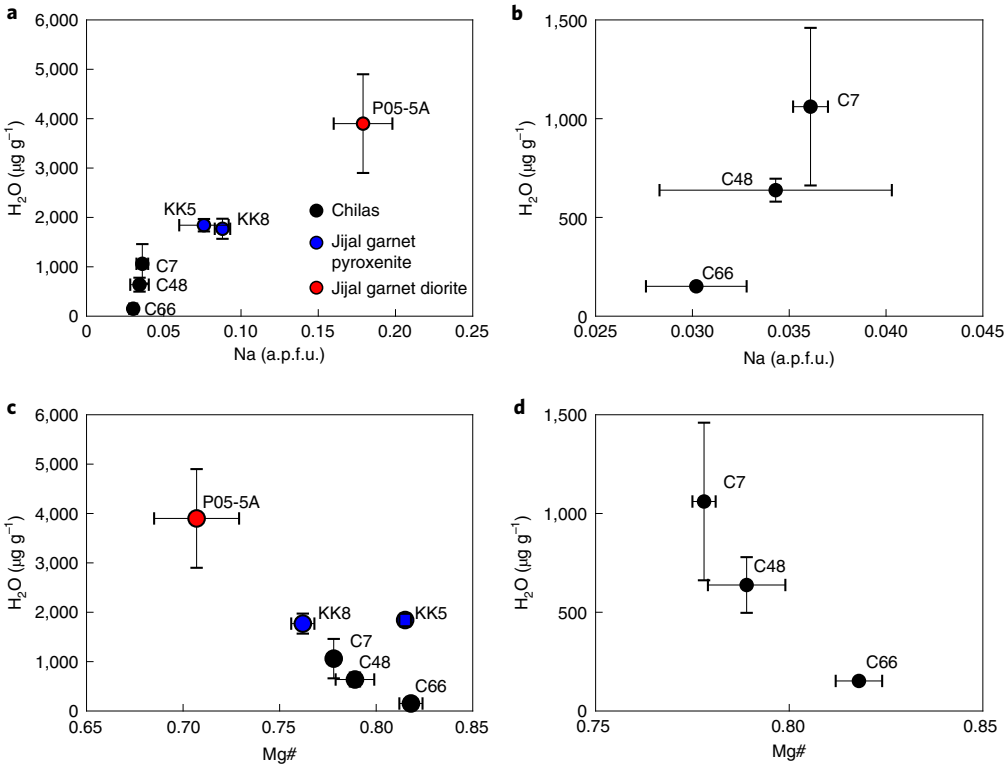

Fig. 1 | Clinopyroxene H_2O abundances plotted against major-element compositions. a,**c**, Data for both the Jijal (blue (garnet pyroxenite) and red (garnet diorite) circles) and Chilas (black circles). **b**,**d**, Data for Chilas only. **a**,**b**, Octahedrally coordinated Na in atoms per formula unit (a.p.f.u.). **c**,**d**, Mg# (molar Mg/(Mg+Fe)). Error bars are 2 s.e.m. Samples are individually labelled; see text for sample description.

(ref. [21].) Primitive Chilas samples crystallized at ~1,200 °C (ref. [22]) and preserve primary igneous textures and compositions on the centimetre scale[23] whereas for Jijal mafic cumulates, crystallization and equilibration temperatures probably extended to lower values according to rare-earth element thermobarometry (T_{REE}; Supplementary Table 1) and experimental constraints[24,25]. The two complexes are composed of a suite of plutonic rocks that crystallized either from hydrous (>4 wt% H_2O) or damp (<2 wt% H_2O) primitive liquids in the Jijal and Chilas complexes, respectively, each following a distinct liquid line of descent (LLD) during differentiation[22,26]. Chilas formed during a period of magmatism at ~80–85 Ma (ref. [27]), while Jijal is thought to have formed slightly earlier (93.9 ± 8.1 Ma, see Supplementary Information for details)[28] with cessation and exhumation of the complex at ~80 Ma (ref. [29]). Jijal exemplifies a typical calc–alkaline (iron depletion trend) differentiation series, whereas Chilas typifies an intermediate to arc tholeiitic arc series[24].

In this study, we investigated three fresh (<5% alteration) gabbronorites from the Chilas Complex (C7, C48, C66) that were previously studied petrologically[22]. Detailed sample descriptions and locations are provided in the Supplementary Information. Mineral assemblages and compositions of the Chilas gabbronorites indicate that the plutonic rocks crystallized from a common parental magma that evolved along a damp LLD[22]. Sample C66, an olivine gabbronorite, is the most primitive sample investigated; C48 and C7 gabbronorites are more evolved and crystallized from a more fractionated melt than C66[22]. Three minimally altered samples (<5% alteration) were also selected from the Jijal Complex, including two garnet pyroxenites (KK5 and KK8) and a garnet diorite (P05-5A). Field observations and experimental constraints suggest that the Jijal garnet pyroxenites and garnet diorite are broadly related[24] along a hydrous LLD. However, in detail, Jijal samples require individual batches of melt to satisfy field, experimental and trace-element constraints[24]. For example, Jijal exhibits deviations from experimentally predicted cumulate assemblages, particularly the juxtaposition of pyroxene–garnet hornblendites and garnet hornblende gabbros, suggesting that multiple magmas (probably with different compositions and H_2O contents) were involved in Jijal genesis[24]. As a result, H_2O abundances in each cumulate series are expected to be vastly different[26].

Preservation of magmatic H_2O abundances in cumulate minerals

In the Chilas gabbronorites, clinopyroxene H_2O abundances range from 152 ± 8 μg g^{-1} (2 s.e.m.) to 1,061 ± 399 μg g^{-1} (Fig. 1). Orthopyroxene and amphibole were also analysed in some of the samples, yielding 102–105 μg g^{-1} and ~2 wt% H_2O, respectively. In the Jijal samples, clinopyroxene contains from 1,770 ± 204 μg g^{-1} H_2O to 3,900 ± 1,000 μg g^{-1} H_2O. Garnet and amphibole were also analysed in some of the samples, yielding 94–167 μg g^{-1} and ~1.8 wt% H_2O, respectively. Data are available in Table 1 and Supplementary Table 2.

Several lines of evidence indicate that magmatic H_2O abundances should have been largely preserved. First, samples are pristine and show no evidence for retrograde overprinting or reaction with metamorphic fluids. This is important because substantial loss or addition of hydrogen in nominally anhydrous minerals is often observed in relation with melt[30–32]. Second, only minimal deviations in H_2O abundances are observed at the clinopyroxene rims compared with cores, inconsistent with transient diffusion profiles of hydrogen[30,33] (Supplementary Fig. 2). However, hydrogen diffusion length over 1 Myr in clinopyroxene can be >10 m at temperatures of 800–1,200 °C (refs. [32,34]), so that hydrogen may have internally re-equilibrated between mineral phases during sub-solidus re-equilibration[35]. Few constraints exist on the effects of sub-solidus re-equilibration of H_2O in lower-crustal lithologies. Nonetheless,

Table 1 | Kohistan clinopyroxene volatile abundances

		Clinopyroxene										
Sample	Description	Number of grains analysed	Number of analyses	H_2O (μg g^{-1})	F (μg g^{-1})	Cl (μg g^{-1})	P (μg g^{-1})	S (μg g^{-1})	Calculated H_2O Dcpx-melt	Calculated parental melt H_2O (wt%)	Calculated primitive melt H_2O (wt%)	Calculated parental melt F (μg g^{-1})	Calculated parental melt Cl (μg g^{-1})
C66	Olivine gabbronorite	2	9	152 ± 8	0.633 ± 0.048	0.036 ± 0.026	13.9 ± 3.1	0.025 ± 0.002	0.0123	1.21 ± 0.09	0.61–0.85	26	12–111
C48	gabbronorite	3	4	638 ± 141	4.16 ± 1.49	0.115 ± 0.020	-	0.049 ± 0.004	0.0193	6.38 ± 0.96	-	238	81–778
C7	gabbronorite	2	6	1,061 ± 399	9.71 ± 5.06	0.390 ± 0.487	13.6 ± 4.0	0.100 ± 0.104	0.0096	10.95 ± 4.09	-	518	160–1,539
KK5	Garnet pyroxenite	2	7	1,770 ± 204	5.68 ± 1.87	0.112 ± 0.089	9.13 ± 0.71	0.016 ± 0.002	0.0148	8.44 ± 0.39	6.0–10.0	139	23–222
KK8	Garnet pyroxenite	3	8	1,842 ± 126	3.40 ± 0.33	0.049 ± 0.027	7.98 ± 1.27	0.023 ± 0.002	0.0123	12.44 ± 0.34	6.0–10.0	119	28–272
P05-5A	Garnet diorite	2	5	3,900 ± 1,000	54.8 ± 16.3	3.09 ± 2.25	-	0.083 ± 0.072	0.0199	19.57 ± 1.49	4.0–5.0	1,404	1,780–17,167

Kohistan clinopyroxene mean volatile abundances (SIMS), including the number of analyses conducted, number of grains analysed per sample, calculated partition coefficients and calculated parental melt characteristics for each sample. Dcpx, clinopyroxene-melt H_2O partition coefficient. Individual analyses available in the Supplementary Information.

H_2O inter-mineral partition coefficients between clinopyroxene and garnet measured in Jijal samples (Supplementary Fig. 3) are consistent with experimental partitioning data at magmatic temperatures (>1,000 °C). The distribution of H_2O between orthopyroxene and clinopyroxene in Chilas samples is similar to what has been observed in other pyroxenites but cannot be compared directly with experiments due to differences in mineralogy (see Supplementary Information for details on inter-mineral partitioning). Last, there is no reverse Mg# zoning in pyroxenes or major- or trace-element rim enrichment that would indicate post-crystallization modification of pyroxene chemistry by late interstitial liquid. Pyroxenes adjacent to amphibole rims have similar H_2O abundances to others. Therefore, mineral H_2O abundances probably reflect preservation of magmatic H_2O contents at the time of crystallization, with cores largely unaffected by diffusive re-equilibration. The same arguments apply for other volatile elements (fluorine and chlorine), although their diffusivities are probably lower because of their larger ionic radii.

Kohistan's tectonic history may have been crucial in preserving near-magmatic H_2O abundances. Evidence from xenoliths highlights the potential for diffusive H_2O loss during magmatic eruptions, where rapid pressure changes and steep geochemical gradients lead to host-magma degassing, xenolith re-equilibration and H_2O loss[34] visible in both olivine and pyroxene at temperatures below 900 °C[33]. In Kohistan, the absence of late fluid metasomatism episodes after cumulate formation, followed by rapid exhumation at ~80–85 Ma, may have contributed to H_2O preservation.

H_2O and halogen abundances in Kohistan parental melts

Preservation of magmatic H_2O abundances in lower-crustal minerals permits the calculation of H_2O abundances in the parental melts from which the cumulates formed at lower-crustal depths. Partition coefficients for hydrogen between clinopyroxene and melt at relevant pressure and temperature conditions have been calibrated empirically from experimental studies[19] and range here from 0.0096 to 0.0199 (Table 1). The most primitive Chilas olivine gabbronorite, C66, yields a parental melt H_2O concentration of 1.21 ± 0.09 wt% (2 s.e.m., n = 9). More-differentiated samples C48 and C7 are in equilibrium with more-hydrous melt compositions with 6.38 ± 0.96 (2 s.e.m., n = 3) and 10.95 ± 4.09 (2 s.e.m., n = 6) wt% H_2O, respectively (Fig. 2). The Jijal garnet pyroxenites KK5 and KK8 yield parental melt H_2O concentrations of 8.44 ± 0.39 (2 s.e.m., n = 5) and 12.44 ± 0.34 (2 s.e.m., n = 6) wt%, respectively, and garnet diorite P05-5A is in equilibrium with a melt that contained 19.6 ± 1.5 wt% H_2O (2 s.e.m., n = 5) (Fig. 2). In addition, calculated F and Cl abundances (Table 1) in super-hydrous melts match the highest halogen abundances recorded by melt inclusions (Fig. 2), suggesting that H_2O is lost from melt inclusions compared with halogens.

Crystal fractionation controls H_2O abundances

The large variability in H_2O abundances measured in cumulate minerals and calculated for the melts in equilibrium with the cumulates can be explained by examining correlations between H_2O and other trace and major elements. During crystallization, H_2O preferentially remains in the melt phase and is incompatible in clinopyroxene[36]. In Chilas, clinopyroxene H_2O abundances increase from the most primitive sample C66 (cpx Mg# 81.8) to progressively more evolved C48 (cpx Mg# 78.9) and C7 (cpx Mg# 77.8) (Fig. 1). In addition, H_2O in clinopyroxene positively correlates with other incompatible elements, such as Ce (and all other rare-earth elements), Zr, F (Fig. 3), Na (Fig. 1) and Ti (Supplementary Fig. 4). Ba and Li concentrations may be higher with increasing cpx H_2O. Sr and H_2O correlate negatively due to the presence of plagioclase (Fig. 3). Plagioclase anorthite content (An#, atomic Ca/(Ca+Na)) in C66 (An# 89.8), C48 (An# 75.0) and C7 (An# 56.4) also displays a negative correlation with clinopyroxene H_2O abundances, consistent with crystal fractionation. Finally, an equilibrium crystallization model[22] for melt

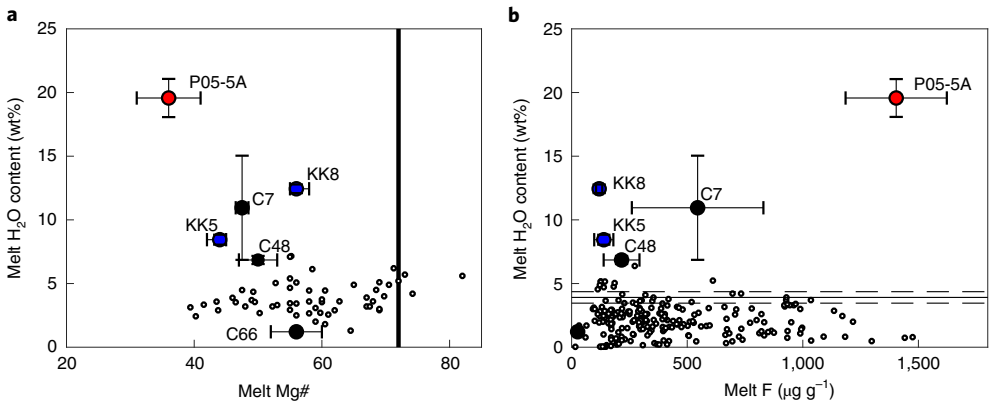

Fig. 2 | Kohistan equilibrium melt H_2O abundances compared to arc magma literature. a. Equilibrium melt H_2O abundances plotted against melt Mg#. Melt Mg# inferred from clinopyroxene Mg# for both Chilas (black circles) and Jijal (blue (garnet pyroxenites) and red (garnet diorite) circles) cumulates. Mg# error bars denote highest and lowest measured clinopyroxene Mg# for each sample, H_2O error bars are 2 s.e.m. Melt-inclusion literature data (white circles) are maximum water abundances for individual arc volcanoes[5] converted from olivine forsterite content to melt Mg#. Thick vertical black line denotes Mg# of melts in equilibrium with mantle olivine Fo_{90} (Mg# 72). **b**. Fluorine and H_2O abundances of arc melt inclusions compared with parental melts calculated for Kohistan. Horizontal line signifies mean H_2O content of arc melts (dashed lines are 1 s.d.) as interpreted from melt inclusions[5]. Olivine-hosted melt-inclusion data for Fig. 2b from the literature[53–56].

Sr/Y ratio (fluid-mobile/fluid-immobile element) and H_2O concentration links the gabbronorite suite from the most primitive sample (C66) to more evolved compositions (C48 and C7) through a single LLD[22] (Fig. 4a and Supplementary Information). Therefore, increasing H_2O abundances in Chilas pyroxenes and parental melts reflect increasing degrees of crystal fractionation from a single primitive melt. The fit between the data and the model also reinforces the hypothesis that H_2O concentrations in clinopyroxene are near magmatic.

In the Jijal samples, clinopyroxene H_2O abundances also increase from the two garnet pyroxenites (Mg# 76.2–81.5) to the more evolved P05-5A garnet diorite (Mg# 70.7). P05-5A has the highest Na clinopyroxene content of the series, consistent with its more evolved nature. Unlike Chilas, the Jijal sample series does not exhibit compelling correlations between H_2O and most other incompatible elements because Jijal cumulates were derived from individual batches of melt[24] and because elements such as high-field-strength elements and rare-earth elements (REEs) were taken up by accessory phases, for example, ilmenite, zircon and apatite (Supplementary Fig. 5). Nonetheless, H_2O positively correlates with fluid-mobile elements F, Ba and Li in Jijal clinopyroxene (Supplementary Fig. 5). In addition, the calculated Sr/Y and H_2O variability of parental melts in equilibrium with Jijal cumulates is consistent with fractional crystallization[22] of individual batches of melts with varying initial H_2O abundances (Fig. 4b) and precipitation of garnet where Y is compatible. Therefore, H_2O variations in Jijal minerals probably reflect varying degrees of crystal fractionation from distinct primitive melts.

Damp to super-hydrous primitive arc melts

The H_2O abundances of primitive melts before extensive crystal fractionation can be back calculated, assuming that H_2O degassing before cumulate formation was negligible. The solubility of H_2O in basaltic melts at 0.4–0.6 GPa is thought to be ~7–11 wt% (refs. [37,38]) and increases with increasing pressure to 20.6 ± 0.9 wt% H_2O (2 s.e.m.) at 1 GPa and 1,200 °C (ref. [2]). Barometry estimates of 0.6–0.7 GPa for Chilas and 0.8–1.5 GPa for Jijal, therefore, suggest that equilibrium melts were probably H_2O-undersaturated and did not degas before cumulate crystallization.

To constrain the H_2O contents of primitive melts for the Chilas complex, an additional fractionation correction is needed (Supplementary Information). On the basis of previous studies[22], it is assumed that parental liquids in equilibrium with the most primitive gabbronorite (C66) were already evolved with an Mg# of ~53 and underwent 30–50% olivine and clinopyroxene fractionation before C66 crystallization. After applying this additional fractionation correction, primitive Chilas melts are inferred to contain 0.61–0.85 wt% H_2O. This range is consistent with primitive tholeiitic melts formed by decompression melting in an intra-arc extensional setting, that is, a damp basaltic parental magma with a minor slab contribution[22,26,39].

Similar to the Chilas complex, Jijal cumulates also formed from melts that underwent prior crystallization. Because of the complexity of Jijal, two independent approaches are used to evaluate H_2O concentrations in primitive melts (Supplementary Information). The first method is based on comparison with crystallization sequences from laboratory experiments, where melts have undergone between 35% and 60% fractional crystallization of olivine and pyroxene before amphibole and garnet saturation[24,25]. As H_2O is highly incompatible in both pyroxene and olivine, this correction is rather insensitive to mineral modes and partition coefficients and yields H_2O abundances in Jijal primitive melts of 3.4–8.0 wt% H_2O for KK5 and KK8. This method cannot be used to evaluate P05-5A due to its evolved nature. The second method is based on a quantitative petrogenetic model of the Jijal liquid line of descent[40], which permits us to explore a range of initial H_2O abundances for each sample (Fig. 5). The presence of moderately fractionated amphibole-bearing garnet pyroxenites in the fractionation sequence as modelled by previous studies[40] places a lower bound on initial melt H_2O abundances of ~3.25 wt%. Modelling results are consistent with primitive melt H_2O abundances of ~4–5 wt% for P05-5A and 6–10 wt% for KK5 and KK8 (Fig. 5). These values support input from a hydrous slab component during flux melting in a mantle wedge[26].

Implications for ore deposit formation and arc H_2O fluxes

Our results show that primitive arc magmas may contain ~0.6–10 wt% H_2O and may reach H_2O saturation of ~20 wt% H_2O after extensive crystal fractionation in the lower arc crust with Cl abundances up to several thousand μg g^{-1} (Fig. 5 and Table 1). The estimated H_2O concentrations in primitive arc magmas from this study are more variable and notably higher than the average

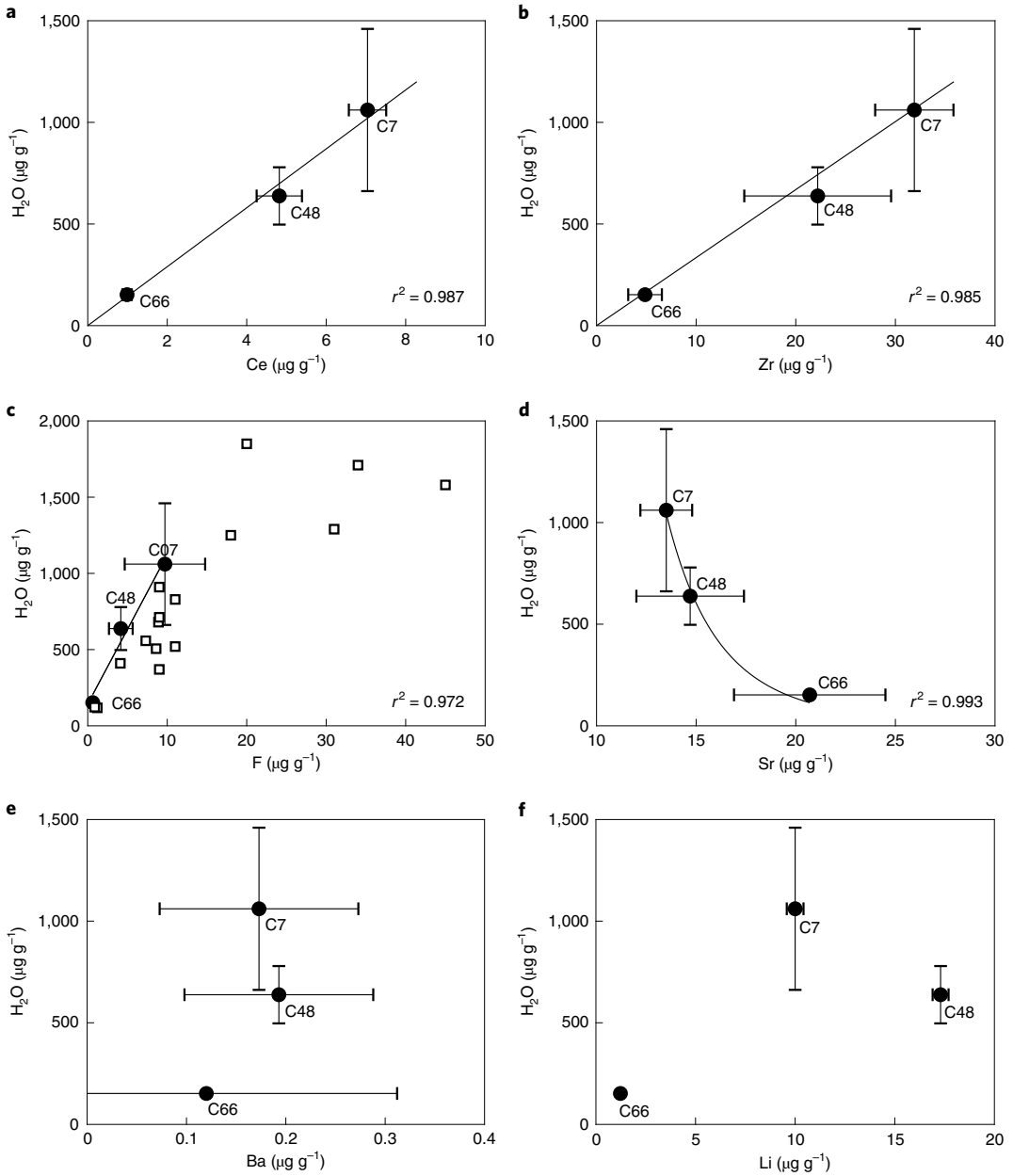

Fig. 3 | Chilas clinopyroxene H_2O concentrations plotted against trace-element concentrations with various geochemical affinities. a, The REE Ce. **b**, The high-field-strength element Zr. **c**, The volatile halogen F. **d**–**f**, The fluid-mobile elements Sr (**d**), Ba (**e**) and Li (**f**). Concentrations are the mean of each sample (clinopyroxene cores only for H_2O). Error bars are 2 s.e.m. White squares denote experimental partitioning data from the literature[19,36]. Black solid lines and curves denote best-fit slopes calculated using MATLAB functions poly1 (**a**–**c**) and power1 (**d**).

of 4 wt% previously inferred from olivine and clinopyroxene-hosted melt inclusions[5] (Figs. 2 and 5b) and support the presence of damp to super-hydrous melts in arc settings[10–12]. The occurrence of super-hydrous, Cl-rich melts under arc roots is important for understanding the formation of ore deposits. Upon magma ascent, H_2O solubility decreases to ~7 wt% at 0.5 Gpa and 950 °C for a basaltic composition (~12 wt% for rhyolite)[41], leading to exsolution of a Cl-rich fluid phase[42]. Exsolved fluids, thought to be important in porphyry Cu, Mo and Au deposit formation[43–45], may be a natural consequence of H_2O exsolution by fractionated, super-hydrous magmas at mid-crustal depths. Such a process is substantiated by mass balance calculations[46], phase equilibria modelling[16] and crystallization experiments[14], all of which implicate H_2O-rich melts (>10 wt%) in the formation of porphyry copper deposits, where exsolution may initiate in the mid-crust. Future work will require parameterizing Cl partitioning behaviour between nominally anhydrous minerals and melt, as copper extraction efficiency during exsolution is highly sensitive to melt Cl concentrations[18].

The andesitic average bulk composition of continental crust may also, in part, be an eventuality of super-hydrous magmas. Crystallization of such magmas at the base of arc crust drives precipitation of thick plagioclase-free, ultramafic sequences, which are seismically indistinguishable from ambient lithospheric mantle[47–50]. Thus, average bulk continental crust estimates using seismic Moho thresholds effectively shift to more evolved (andesitic) compositions[51,52]. Finally, foundering of hydrated lower arc crust will deliver H_2O fluxes back to the mantle and impact global volatile cycling.

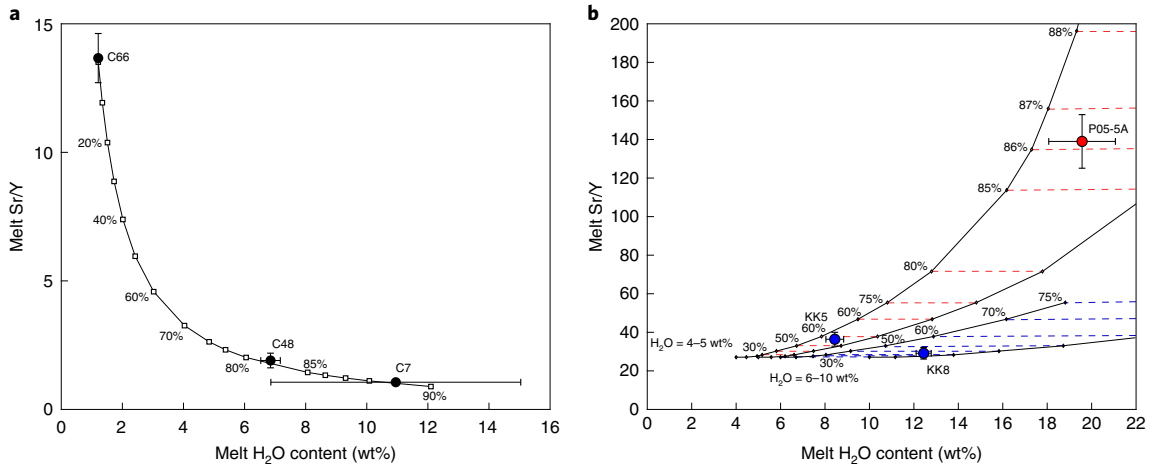

Fig. 4 | Crystallization models for Chilas and Jijal. a, Equilibrium crystallization model (white squares) for Chilas gabbronorites showing the evolution of Sr/Y ratios against H_2O abundances in melts. Upon continued crystallization of plagioclase, Sr decreases as it is compatible in plagioclase, whereas Y increases, being incompatible in all crystallizing phases. Values along curves are percentage crystallization. Parental melt has an H_2O concentration of 1.21 wt% and is the melt parental to C66. **b**. Fractional crystallization models[40] for Jijal cumulates showing the evolution of Sr/Y ratios against varying initial H_2O abundances in melts. The fitted range of H_2O contents in parental melts varies from 4 to 10 wt% H_2O. Dashed blue and red lines are tie lines connecting identical extents of crystallization for different starting melt H_2O abundances (Red: 4 and 5 wt.% H_2O, blue: 6 and 10 wt.% H_2O). Error bars are 2 s.e.m. For details of the two models, see Supplementary Information.

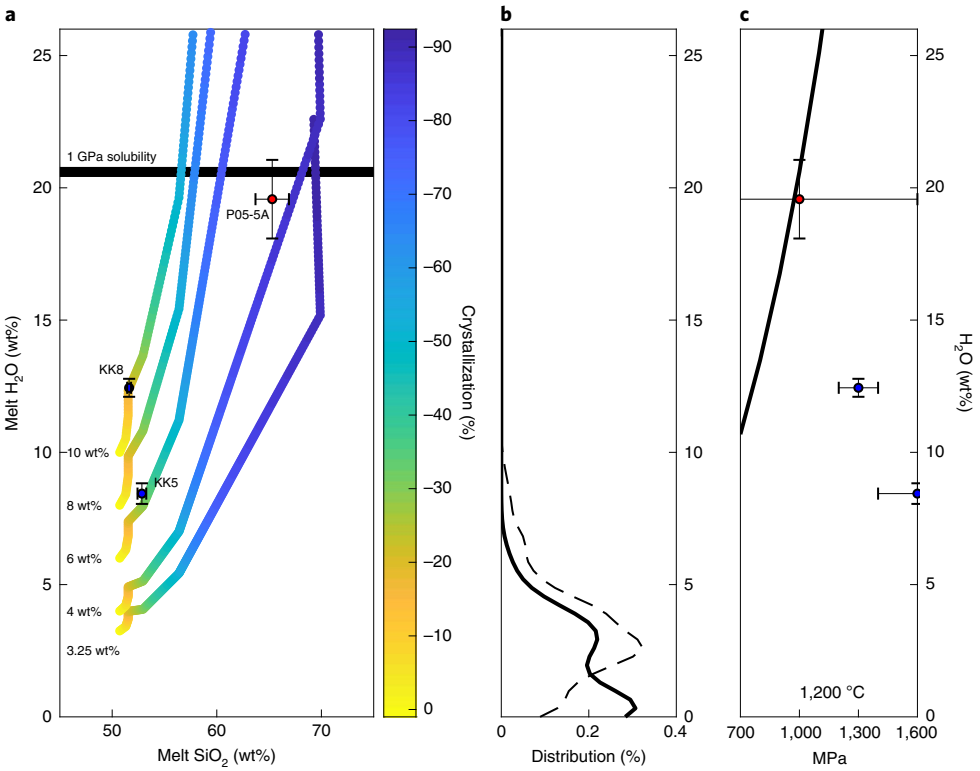

Fig. 5 | Jijal crystallization model. a, Jijal melt crystallization model based on published petrogenetic model[40]. Equilibrium melt SiO_2 content for each sample calculated on the basis of clinopyroxene Mg# using modelled LLD. Thick black line denotes 1 GPa H_2O solubility for a basaltic melt[2]. Silicic magmas tend to have higher water solubilities than basalt; however, constraints at relevant pressure and temperature conditions are lacking. Values next to each curve represent the range of H_2O abundances in parental melts, with the lower bound constrained by the minimum amount of water needed to crystallize amphibole in the fractionation sequence[40], that is, 3.25 wt% H_2O. See Supplementary Information for details. *y*-axis error bars are 2 s.e.m.; *x*-axis error bars are 2 s.e.m. of modelled melt SiO_2 content calculated from the range of Cpx Mg# found in each sample. **b**, Probability density function of mineral-hosted arc melt inclusions from the GEOROC Database[57]. Primitive melt inclusions (Mg# > 65) are shown as a solid back line (n=171). Melt inclusions with Mg# of 35 to 65 (n=879), similar to the Mg# calculated for Kohistan parental melts, are shown as a dashed black line. Primitive melt inclusions (solid black line) display two probability peaks at 0.3 and 2.3 wt% H_2O with a maximum H_2O of 4.8 wt%, whereas those with an Mg# of 35 to 65 show a single peak at 2.0 wt% H_2O and a maximum of 7.5 wt% H_2O. **c**, H_2O solubility curve for basaltic melts at 1,200 °C[2] compared with calculated melt H_2O abundances for Jijal cumulates based on thermobarometry (Supplementary Table 1). *y*-axis error bars are 2 s.e.m.; *x*-axis error bars are 1σ based on the Cpx-garnet barometer of ref. [58].

The hydrated lower arc crust can therefore modulate volatile cycling between the crust and mantle.

Online content

Any methods, additional references, Nature Research reporting summaries, source data, extended data, supplementary information, acknowledgements, peer review information; details of author contributions and competing interests; and statements of data and code availability are available at https://doi.org/10.1038/s41561-022-00947-w.

Received: 24 August 2020; Accepted: 14 April 2022;
Published online: 26 May 2022

References

1. Wallace, P. J., Plank, T., Edmonds, M. & Hauri, E. H. in *The Encyclopedia of Volcanoes* (ed. Sigurdsson, H.) 163–183 (Elsevier, 2015).
2. Mitchell, A. L., Gaetani, G. A., O'Leary, J. A. & Hauri, E. H. H_2O solubility in basalt at upper mantle conditions. *Contrib. Miner. Petrol.* **172**, 85 (2017).
3. Dobson, P. F., Skogby, H. & Rossman, G. R. Water in boninite glass and coexisting orthopyroxene: concentration and partitioning. *Contrib. Mineral. Petrol.* **118**, 414–419 (1995).
4. Sisson, T. & Layne, G. H_2O in basalt and basaltic andesite glass inclusions from four subduction-related volcanoes. *Earth Planet Sci. Lett.* **117**, 619–635 (1993).
5. Plank, T., Kelley, K. A., Zimmer, M. M., Hauri, E. H. & Wallace, P. J. Why do mafic arc magmas contain ~4 wt% water on average? *Earth Planet Sci. Lett.* **364**, 168–179 (2013).
6. Gaetani, G. A., O'Leary, J. A., Shimizu, N., Bucholz, C. E. & Newville, M. Rapid reequilibration of H_2O and oxygen fugacity in olivine-hosted melt inclusions. *Geology* **40**, 915–918 (2012).
7. Portnyagin, M., Almeev, R., Matveev, S. & Holtz, F. Experimental evidence for rapid water exchange between melt inclusions in olivine and host magma. *Earth Planet Sci. Lett.* **272**, 541–552 (2008).
8. Bucholz, C. E., Gaetani, G. A., Behn, M. D. & Shimizu, N. Post-entrapment modification of volatiles and oxygen fugacity in olivine-hosted melt inclusions. *Earth Planet. Sci. Lett.* **374**, 145–155 (2013).
9. Annen, C., Blundy, J. & Sparks, R. The genesis of intermediate and silicic magmas in deep crustal hot zones. *J. Petrol.* **47**, 505–539 (2006).
10. Goltz, A. E., Krawczynski, M. J., Gavrilenko, M., Gorbach, N. V. & Ruprecht, P. Evidence for superhydrous primitive arc magmas from mafic enclaves at Shiveluch volcano, Kamchatka. *Contrib. Mineral. Petrol.* **175**, 115 (2020).
11. Grove, T. L. et al. Magnesian andesite and dacite lavas from Mt. Shasta, northern California: products of fractional crystallization of H_2O-rich mantle melts. *Contrib. Mineral. Petrol.* **148**, 542–565 (2005).
12. Krawczynski, M. J., Grove, T. L. & Behrens, H. Amphibole stability in primitive arc magmas: effects of temperature, H_2O content, and oxygen fugacity. *Contrib. Mineral. Petrol.* **164**, 317–339 (2012).
13. Zellmer, G. F. et al. Petrogenesis of antecryst-bearing arc basalts from the trans-Mexican volcanic belt: insights into along-arc variations in magma-mush ponding depths, H_2O contents, and surface heat flux. *Am. Mineral.* **101**, 2405–2422 (2016).
14. Prouteau, G. & Scaillet, B. Experimental constraints on the origin of the 1991 Pinatubo dacite. *J. Petrol.* **44**, 2203–2241 (2003).
15. Carmichael, I. S. The andesite aqueduct: perspectives on the evolution of intermediate magmatism in west-central (105–99° W) Mexico. *Contrib. Mineral. Petrol.* **143**, 641–663 (2002).
16. Lu, Y.-J., Loucks, R. R., Fiorentini, M. L., Yang, Z.-M. & Hou, Z.-Q. Fluid flux melting generated postcollisional high Sr/Y copper ore–forming water-rich magmas in Tibet. *Geology* **43**, 583–586 (2015).
17. Laumonier, M., Gaillard, F., Muir, D., Blundy, J. & Unsworth, M. Giant magmatic water reservoirs at mid-crustal depth inferred from electrical conductivity and the growth of the continental crust. *Earth Planet. Sci. Lett.* **457**, 173–180 (2017).
18. Tattitch, B., Chelle-Michou, C., Blundy, J. & Loucks, R. R. Chemical feedbacks during magma degassing control chlorine partitioning and metal extraction in volcanic arcs. *Nat. Commun.* **12**, 1774 (2021).
19. O'Leary, J. A., Gaetani, G. A. & Hauri, E. H. The effect of tetrahedral Al^{3+} on the partitioning of water between clinopyroxene and silicate melt. *Earth Planet. Sci. Lett.* **297**, 111–120 (2010).
20. Tahirkheli, R. A. K. & Jan, M. Q. Geology of Kohistan, Karakorum Himalaya, northern Pakistan. *Geol. Bull. Univ. Peshawar* **11**, 1–30 (1979).
21. Jagoutz, O. & Schmidt, M. W. The formation and bulk composition of modern juvenile continental crust: the Kohistan arc. *Chem. Geol.* **298**, 79–96 (2012).
22. Jagoutz, O. et al. Petrology and mineral chemistry of lower crustal intrusions: the Chilas Complex, Kohistan (NW Pakistan). *J. Petrol.* **48**, 1895–1953 (2007).
23. Loucks, R. R. Restoration of the elemental and stable-isotopic compositions of diffusionally altered minerals in slowly cooled rocks. *Contrib. Mineral. Petrol.* **124**, 346–358 (1996).
24. Müntener, O. & Ulmer, P. Arc crust formation and differentiation constrained by experimental petrology. *Am. J. Sci.* **318**, 64–89 (2018).
25. Ulmer, P., Kaegi, R. & Müntener, O. Experimentally derived intermediate to silica-rich arc magmas by fractional and equilibrium crystallization at 1·0 GPa: an evaluation of phase relationships, compositions, liquid lines of descent and oxygen fugacity. *J. Petrol.* **59**, 11–58 (2018).
26. Jagoutz, O., Muntener, O., Schmidt, M. W. & Burg, J. P. The roles of flux- and decompression melting and their respective fractionation lines for continental crust formation: evidence from the Kohistan arc. *Earth Planet Sci. Lett.* **303**, 25–36 (2011).
27. Schaltegger, U., Zeilinger, G., Frank, M. & Burg, J. P. Multiple mantle sources during island arc magmatism: U–Pb and Hf isotopic evidence from the Kohistan arc complex, Pakistan. *Terra Nova* **14**, 461–468 (2002).
28. Bouilhol, P., Jagoutz, O., Hanchar, J. M. & Dudas, F. O. Dating the India–Eurasia collision through arc magmatic records. *Earth Planet. Sci. Lett.* **366**, 163–175 (2013).
29. Burg, J. P., Jagoutz, O., Dawood, H. & Hussain, S. S. Precollision tilt of crustal blocks in rifted island arcs: structural evidence from the Kohistan Arc. *Tectonics* **25**, TC5005 (2006).
30. Demouchy, S., Jacobsen, S. D., Gaillard, F. & Stern, C. R. Rapid magma ascent recorded by water diffusion profiles in mantle olivine. *Geology* **34**, 429–432 (2006).
31. Le Roux, V. et al. Postmelting hydrogen enrichment in the oceanic lithosphere. *Sci. Adv.* **7**, eabf6071 (2021).
32. Peslier, A. H. & Luhr, J. F. Hydrogen loss from olivines in mantle xenoliths from Simcoe (USA) and Mexico: mafic alkalic magma ascent rates and water budget of the sub-continental lithosphere. *Earth Planet. Sci. Lett.* **242**, 302–319 (2006).
33. Xu, Y. et al. Reconciling the discrepancy between the dehydration rates in mantle olivine and pyroxene during xenolith emplacement. *Geochim. Cosmochim. Acta* **267**, 179–195 (2019).
34. Ferriss, E., Plank, T. & Walker, D. Site-specific hydrogen diffusion rates during clinopyroxene dehydration. *Contrib. Mineral. Petrol.* **171**, 55 (2016).
35. Schaffer, L. A. et al. Effects of melting, subduction-related metasomatism, and sub-solidus equilibration on the distribution of water contents in the mantle beneath the Rio Grande Rift. *Geochim. Cosmochim. Acta* **266**, 351–381 (2019).
36. Hauri, E. H., Gaetani, G. A. & Green, T. H. Partitioning of water during melting of the Earth's upper mantle at H_2O-undersaturated conditions. *Earth Planet Sci. Lett.* **248**, 715–734 (2006).
37. Berndt, J. et al. A combined rapid-quench and H_2-membrane setup for internally heated pressure vessels: description and application for water solubility in basaltic melts. *Am. Mineral.* **87**, 1717–1726 (2002).
38. Hamilton, D., Burnham, C. W. & Osborn, E. The solubility of water and effects of oxygen fugacity and water content on crystallization in mafic magmas. *J. Petrol.* **5**, 21–39 (1964).
39. Jagoutz, O., Müntener, O., Burg, J.-P., Ulmer, P. & Jagoutz, E. Lower continental crust formation through focused flow in km-scale melt conduits: the zoned ultramafic bodies of the Chilas Complex in the Kohistan island arc (NW Pakistan). *Earth Planet. Sci. Lett.* **242**, 320–342 (2006).
40. Jagoutz, O. E. Construction of the granitoid crust of an island arc. Part II: a quantitative petrogenetic model. *Contrib. Mineral. Petrol.* **160**, 359–381 (2010).
41. Newman, S. & Lowenstern, J. B. VolatileCalc: a silicate melt–H_2O–CO_2 solution model written in Visual Basic for Excel. *Comput. Geosci.* **28**, 597–604 (2002).
42. Alletti, M. et al. Chlorine partitioning between a basaltic melt and H_2O–CO_2 fluids at Mount Etna. *Chem. Geol.* **263**, 37–50 (2009).
43. Lee, C.-T. A. & Tang, M. How to make porphyry copper deposits. *Earth Planet. Sci. Lett.* **529**, 115868 (2020).
44. Hedenquist, J. W., Arribas, A. & Reynolds, T. J. Evolution of an intrusion-centered hydrothermal system; Far Southeast-Lepanto porphyry and epithermal Cu-Au deposits, Philippines. *Econ. Geol.* **93**, 373–404 (1998).
45. Rezeau, H. & Jagoutz, O. The importance of H_2O in arc magmas for the formation of porphyry Cu deposits. *Ore Geol. Rev.* **126**, 103744 (2020).
46. Klemm, L. M., Pettke, T. & Heinrich, C. A. Fluid and source magma evolution of the Questa porphyry Mo deposit, New Mexico, USA. *Miner. Depos.* **43**, 533 (2008).
47. Loucks, R. R. Deep entrapment of buoyant magmas by orogenic tectonic stress: its role in producing continental crust, adakites, and porphyry copper deposits. *Earth Sci. Rev.* **220**, 103744 (2021).
48. Kodaira, S. et al. Seismological evidence for variable growth of crust along the Izu intraoceanic arc. *J. Geophys. Res. Solid Earth* **112**, B05104 (2007).
49. Kodaira, S. et al. New seismological constraints on growth of continental crust in the Izu-Bonin intra-oceanic arc. *Geology* **35**, 1031–1034 (2007).

50. Behn, M. D. & Kelemen, P. B. Stability of arc lower crust: insights from the Talkeetna arc section, south central Alaska, and the seismic structure of modern arcs. *J. Geophys. Res. Solid Earth* **111**, B11207 (2006).
51. O'Reilly, S. Y. & Griffin, W. Moho vs crust–mantle boundary: evolution of an idea. *Tectonophysics* **609**, 535–546 (2013).
52. Müntener, O. & Ulmer, P. Experimentally derived high-pressure cumulates from hydrous arc magmas and consequences for the seismic velocity structure of lower arc crust. *Geophys. Res. Lett.* **33**, L21308 (2006).
53. Portnyagin, M., Hoernle, K., Plechov, P., Mironov, N. & Khubunaya, S. Constraints on mantle melting and composition and nature of slab components in volcanic arcs from volatiles (H_2O, S, Cl, F) and trace elements in melt inclusions from the Kamchatka Arc. *Earth Planet Sci. Lett.* **255**, 53–69 (2007).
54. Rose-Koga, E. F. et al. Volatile (F and Cl) concentrations in Iwate olivine-hosted melt inclusions indicating low-temperature subduction. *Earth Planets Space* **66**, 81 (2014).
55. Rose-Koga, E. F. et al. Mantle source heterogeneity for South Tyrrhenian magmas revealed by Pb isotopes and halogen contents of olivine-hosted melt inclusions. *Chem. Geol.* **334**, 266–279 (2012).
56. Sadofsky, S. J., Portnyagin, M., Hoernle, K. & van den Bogaard, P. Subduction cycling of volatiles and trace elements through the Central American volcanic arc: evidence from melt inclusions. *Contrib. Mineral. Petrol.* **155**, 433–456 (2008).
57. *GEOROC Compilation: Melt Inclusions*. Goettingen Research Online 1 (DIGIS, accessed 24 June 2020); http://georoc.mpch-mainz.gwdg.de/georoc/
58. Sun, C. & Liang, Y. A REE-in-garnet-clinopyroxene thermobarometer for eclogites, granulites and garnet peridotites. *Chem. Geol.* **393–394**, 79–92 (2015).

Methods

Analytical techniques. *Workflow.* We performed SIMS analyses first as electron microprobe (EMPA) carbon coating remains could affect data quality for SIMS analyses. Next, EMPA spots were conducted in a four-point pattern: to the north, south, east and west of the SIMS spot, within ~10–20 µm. In cases when this was not possible (due to surface imperfections and so on) we still made at least two EMPA analyses on the inward (core) and outward (rim) side of each SIMS spot. These values were then averaged for the purposes of comparing SIMS and EMPA data. Laser ablation data for Chilas have been published previously[22], so the mineral average (minimum of eight spots) was used for a given sample. Laser ablation data for Jijal was conducted on the core, middle and rim of each mineral grain; due to rim heterogeneity, rims were excluded to compare with volatile data. To meaningfully compare, Table 1 and Supplementary Table 2 display SIMS volatile abundances measured on the core and middle to define mineral averages for each sample.

SIMS. SIMS analyses (Table 1 and Supplementary Tables 2 and 4) were conducted at the Northeast National Ion Microprobe facility at Woods Hole Oceanographic Institution on a Cameca 1280. A detailed sample protocol may be found in previous studies[59]; here we discuss additional protocols built on that work. Calibration slopes (m) were obtained by plotting measured isotope ratios (x) against known reference material concentrations (y) of the form $y = mx$ for each element of interest. Sample unknowns were then calculated by multiplying measured ratios by m. Calibration slope uncertainties were assessed utilizing a bootstrapping technique (5,000 iterations) to derive 95% confidence intervals. Calibration slopes for each element, mineral and session are shown in Supplementary Fig. 6. Water and F measurements where the internal precision (2 s.e.m. over five counting cycles) was greater than 20% were screened and excluded from the dataset; these low-precision measurements were associated with elevated C (not reported) and Cl concentrations and are probably the result of analyses conducted on micro-fractures. After screening, analytical uncertainties (internal precision: typically 2 s.e.m. ~2% H_2O, <2% F, <7% Cl) were combined with calibration slope uncertainties (accuracy: typical uncertainty 4% H_2O, 2.5% F, <9% Cl, 95% confidence intervals) to yield no more than 15%, 30% and 31% total uncertainty (2 s.e.m., 95% confidence intervals) for H_2O, F and Cl measurements, respectively. We note that propagated 2 s.e.m. uncertainties were typically much lower, for example, ~5%, 7% and 16%, for H_2O, F and Cl (Supplementary Table 4). The cpx and orthopyroxene (opx) volatile standards of ref. [60] were utilized for H_2O, F and P. Since mineral-specific calibrations are not well constrained and/or not available for volatiles in garnet and amphibole, or for S and Cl in pyroxenes, we used a basaltic glass calibration (Supplementary Fig. 6). Continuous measurements of ALV519-4-1 were used throughout the session to monitor instrument drift, which was found to be negligible. The H_2O and F, and Cl concentrations of Suprasil 102 (Heraeus Tenevo LLC), an optical-quality glass, and synthetic forsterite were measured regularly in each session. There are no published values for the H_2O, F and Cl contents of Suprasil (H_2O and F) and synthetic forsterite (Cl), but those samples are believed to have very low H_2O, F and Cl concentrations (<1 µg g^{-1}). To quantify our maximum backgrounds, we assume that Suprasil contains no H_2O or F and synthetic forsterite contains no Cl. A time-interpolated background correction was used for sample C66 (Supplementary Table 6). All other background H_2O, F and Cl values were less than 3 µg g^{-1}, 0.15 µg g^{-1} and 0.09 µg g^{-1}, respectively, for all sessions. Individual mineral analyses were not corrected for background when background values were less than propagated 2 s.e.m. uncertainty; otherwise, measurements are corrected to remove backgrounds. We recommend that the measured H_2O contents of Suprasil 102 be conservatively multiplied by 1.85 for opx background and multiplied by 1.95 for cpx background, reflecting the average difference in Si content between the pyroxene and glasses[31]. For example, if the Suprasil background is ~5 µg g^{-1}, it means that the real background is ~9 µg g^{-1} for an opx and ~10 µg g^{-1} for a cpx. Cl measurement uncertainties on some cpx, opx and garnet are near parity with synthetic forsterite Cl values. We therefore subtracted our background Cl values from measured values for all values presented in tables. Sulfur and phosphorus concentrations were not background corrected.

Electron microprobe and major-element zonation. Major-element compositions of mineral phases were analysed by EMPA using a JEOL JXA-8200 at the Massachusetts Institute of Technology and are available in Supplementary Table 4. A 1 nA beam current and 15 kV accelerating potential were used for all analyses except apatite, which utilized a 10 nA beam current. Beam diameter was <1 µm for cpx, garnet and opx and 10 µm for amphibole. Data reduction was done using CITZAF software (Armstrong 1995). The counting times used for phase analysis was 40 s on peak and 20 s on background. With respect to halogen abundances in amphibole, detection limits based on counting statistics were ~470 µg g^{-1} for F and ~60 µg g^{-1} for Cl.

Oxide compositions in weight percent were converted to atoms per formula unit. The Mg# of Chilas clinopyroxenes ranges from 81.8 (C66) to 77.8 (C7). Total aluminium ranges from 0.127 (C48 and C7) to 0.154, tetrahedrally coordinated Al ($^{IV}Al^{3+}$) from 0.104 (C66) to 0.69 (C7) and octahedrally coordinated Al ($^{VI}Al^{3+}$) from 0.051 (C66) to 0.058 (C7). Measured H_2O concentrations correlate negatively with Mg# as expected for crystal fractionation and positively with Na^{1+}, Ti^{4+} and $^{VI}Al^{3+}$. Jijal clinopyroxenes span a similar Mg# domain of 0.815 (KK8) to 0.707 (P05-5A). Jijal clinopyroxenes are overall more aluminious than Chilas, with respect to total aluminium (0.252 to 0.36), $^{IV}Al^{3+}$ (0.137 to 0.186) and $^{VI}Al^{3+}$ (0.115 to 0.195). Jijal clinopyroxenes are also more sodic, with Na contents of 0.076 (KK8) to 0.179 (P05-5A) compared with Chilas with 0.030 (C66) to 0.036 (C7).

Analysed minerals are homogeneous in major-element compositions, whereas others display minor intragrain mineral zonation. In Chilas, C66 cpx show decreases in TiO_2 from core (0.37 wt%) to rim (0.25 wt%). P05-5A clinopyroxenes show slight rim enrichments (~0.39 wt%) in Al_2O_3 with respect to cores (~0.35 wt%). Garnet in KK5 and KK8 becomes more almandine rich (<5% change) from core to rim, whereas in P05-5A it becomes more grossular from core to rim (<5% change). To overcome the uncertainties introduced by this minor zonation, we calculated equilibrium melts for each SIMS analysis then took the average for each sample using the same methodology as for laser-induced inductively coupled mass spectrometry (LA-ICP-MS) (see the following and ref. [22]).

LA-ICP-MS and trace-element zonation. Trace-element compositions of minerals have been acquired by LA-ICP-MS and are available in Supplementary Table 5. Data for Chilas had been published previously[22,61].

For KK5 and KK8 samples, minerals (cpx, garnet, amphibole) in polished thin sections were analysed with a Geolas 200 M 193 nm ArF excimer laser coupled with an Elan 6100 DRC quadrupole ICP-MS (LA-ICP-MS) at the University of Lausanne (Switzerland). The performance of the LA-ICP-MS was tested with SRM 612 glass from the National Institute of Standards and Technology (NIST) to improve the sensibility (Mg > 10,000 cps and La > 60,000 cps) and to minimize doubly charged ions (Ba/Ba^{2+} <3%) and oxide production rates (Th/ThO < 0.5%). The laser system allows optimization of the beam size for analysis (20–100 µm), adjusted via an aperture in the beam path, with a frequency of 10 hz and energy of 140 mJ (equivalent to ~10 J cm^{-2} on-sample fluence). Helium was used as the cell gas. The acquisition times for background and ablation interval were ~60 s and 10–25 s, respectively. Dwell times per isotope ranged from 10 to 20 ms, and peak-hopping mode was employed. Absolute trace-element and REE concentrations were then determined using CaO (determined by electron microprobe) as internal standard and SRM 612 glass from NIST as external standard. The average element abundances in SRM 612 were taken from ref. [62]. The data reduction and calculation employed the Lamtrace software[63].

For P05-5A, garnet and clinopyroxene were analysed in polished thick section (150 µm thickness) utilizing an ASI RESOlution excimer laser (193 nm) fed to a Thermo Scientific iCAP Q quadrupole ICP-MS at the Woods Hole Oceanographic Institution. Analyses were performed with a 5 Hz repetition rate and 2 J cm^{-2} fluence on 100 µm spots. Total dwell time was 120 s with 30 s of background on both the front and back end of each analysis. Gas flows were 5 ml min^{-1} (N_2), 500 ml min^{-1} (He) and 1 l min^{-1} (Ar). NIST-612, BCR-2G, BIR-1G and BHVO-2G were used as reference materials to generate a calibration slope for each isotope of interest. Data were reduced using the software package of ref. [64] (Rice University).

Trace-element zonation is observed in some Jijal samples (Supplementary Table 5). In KK8, clinopyroxene shows rim depletions with respect to cores of 20–40% for REE, whereas garnet in the same sample shows core-to-rim variations of <5% for REE. In KK5, minor (<10%) zonation was observed for all phases. P05-5A exhibits more-pronounced REE rim depletions in cpx, with rims lower by a factor of two to eight, particularly for light REE (LREE) and middle REE (MREE). P05-5A garnet shows rim depletions in LREE of approximately 20%, whereas heavy REE (HREE) are enriched in garnet rims by a factor of two with respect to cores. A plot of REE in cpx for all samples is presented in Supplementary Fig. 7.

Calculation of clinopyroxene partition coefficients. Partition coefficients were calculated for each SIMS analysis on the basis of clinopyroxene major-element chemistry using an empirical calibration (ref. [19], equation 10), which is insensitive to pressure and temperature. Specifically, the equation is based on the tetrahedrally coordinated Al content of the clinopyroxene in atoms per formula unit and Ca content in atoms per formula unit.

The fluorine content of Kohistan equilibrium melts was calculated on the basis of the relationship between F and H_2O in individual clinopyroxene, with a $D^{F}_{cpx-melt}/D^{H_2O}_{cpx-melt}$ of 1.93 from experimental studies[19,36] (Table 1). This yields $D^{F}_{cpx-melt}$ values of 0.019 to 0.041. Chlorine partitioning between clinopyroxene and melt is not well constrained. We therefore calculated a range of equilibrium melt Cl concentrations to bracket lower and upper bounds. As a lower bound, we used experiment #1446 (1.5 GPa, 1,050 °C) of ref. [36], which is to multiply saturated with clinopyroxene, amphibole and mica. The cpx and melt contain <1 µg g^{-1} and 576 µg g^{-1} Cl, respectively, for a maximum $D^{Cl}_{cpx-melt}$ of 0.001736 (Table 1). An upper bound for equilibrium melt Cl concentrations was calculated using the Cl inter-mineral partition coefficient between olivine and cpx of 1.1 (ref. [65]) and an olivine-melt partition coefficient of 0.00016 (ref. [66]) for a final $D^{Cl}_{cpx-melt}$ of 0.00018. Dual methods were chosen due to differences in F/Cl ratios arising in experimental data[67], which are far lower than those observed in natural samples[65].

Crystal fractionation models. The model utilizes an equilibrium crystallization model with mineral-melt partition coefficients and modal abundances (10/60/30 cpx/plagioclase/opx) determined previously[22]. The starting melt composition is in equilibrium with the most primitive olivine gabbronorite (C66), where cpx shows no Sr or Eu anomalies and thus preceded plagioclase fractionation. For

Fig. 4a, we show H_2O concentrations plotted against Sy/Y ratios. The model tracks fractionation of Sr (fluid mobile) and Y (fluid immobile), using the same modal abundances as in the preceding. For detailed model parameters (for example, partition coefficients), see Supplementary Table 6. Whereas a previous model required an interstitial liquid[22], this model reproduces trace-element abundances through crystal fractionation only, albeit at a higher degree of crystallization. For example, C48 was previously thought to form after ~60% crystallization, with 2–7% interstitial liquid. The new equilibrium model yields ~80% crystallization with no interstitial liquid and is more consistent with petrographic observations.

The Jijal fractional crystallization model presented in Fig. 4b is identical to previously published models[40] with respect to Sr and Y. In summary, a diverse suite of lithologies from primitive dunites and wehrlites through diorites was analysed from Jijal. Measured bulk rock compositions are fractionated from a starting liquid at each step to achieve a single fractionation sequence to reproduce the observed liquid line of descent. Adding to this, we vary the initial H_2O content of the melts to explore melt evolution. Notably, the Chilas and Jijal models behave inversely. This is due to plagioclase fractionation taking up Sr in Chilas whereas in Jijal, Y is compatible in garnet, yielding increasing Sr/Y ratios as the melt evolves.

Fractionation correction. Chilas gabbronorites are thought to have undergone crystallization before the onset of plagioclase formation of 30–50%, having crystallized olivine and clinopyroxene in an approximate 70:30 proportion. Thus, we back calculated the composition of the initial primitive mantle melt on the basis of a fractional crystallization model using partition coefficients for olivine and clinopyroxene of 0.00126 and 0.0126, respectively. The former was taken from previously published[36] experiment B330, which was conducted at 1.2 GPa and 1,200 °C. The latter was calculated on the basis of the average $Al_{(IV)}$ and Ca content of clinopyroxenes from olivine websterites (C03-43,C03-44,C03-45)[22] and the previously published parameterization[19].

Two methods were used for Jijal. First, a correction was made for fractionation of Jijal garnet pyroxenites, assuming 35–60% fractionation of ultramafics (olivine + pyroxene, using modes and partition coefficients from the preceding) before the onset of amphibole saturation on the basis of experimental studies[24,25]. Second, we utilize the quantitative petrogenetic model of ref. [40] to evaluate a range of initial melt H_2O abundances. We assume that H_2O in each lithology's bulk composition is the difference of the oxide sum from 100 and track the evolution of the melt H_2O content. To generate Fig. 5, the cpx Mg# of each sample was used to calculate the equilibrium melt Mg#, and further the SiO_2 content of the liquid with which it is in equilibrium, on the basis of the previously modelled fractionation sequence[40].

Data availability

All data that support the findings of this study are presented herein or cited in the text and Methods. Arc melt-inclusion data for Fig. 5b were downloaded from the GEOROC Database (http://georoc.mpch-mainz.gwdg.de/georoc/) on 24 June 2020 as a precompiled file MELT_INCLUSIONS.csv and sorted. Geochemical data from this study available at PetDB, https://doi.org/10.26022/IEDA/112279.

Code availability

Code used in the generation of figures is available by request to the corresponding author.

References

59. Urann, B. M., Le Roux, V., John, T., Beaudoin, G. M. & Barnes, J. D. The distribution and abundance of halogens in eclogites: an in situ SIMS perspective of the Raspas Complex (Ecuador). *Am. Mineral.* **105**, 307–318 (2020).
60. Kumamoto, K. M., Warren, J. M. & Hauri, E. H. New SIMS reference materials for measuring water in upper mantle minerals. *Am. Mineral.* **102**, 537–547 (2017).
61. Abers, G. A. & Hacker, B. R. A MATLAB toolbox and Excel workbook for calculating the densities, seismic wave speeds, and major element composition of minerals and rocks at pressure and temperature. *Geochem. Geophys. Geosyst.* **17**, 616–624 (2016).
62. Pearce, N. J. et al. A compilation of new and published major and trace element data for NIST SRM 610 and NIST SRM 612 glass reference materials. *Geostand. Newsl.* **21**, 115–144 (1997).
63. Jackson, S. E. LAMTRACE data reduction software for LA-ICP-MS. *Mineral. Assoc. Can. Short Course Ser.* **40**, 305–307 (2008).
64. Lee, C.-T. A. *Laser Ablation ICP-MS: Data Reduction* (2006); www.cintylee.org/s/LASERABLATIONICP.pdf
65. Urann, B. et al. Fluorine and chlorine in mantle minerals and the halogen budget of the Earth's mantle. *Contrib. Mineral. Petrol.* **172**, 51 (2017).
66. Joachim, B. et al. Effect of water on the fluorine and chlorine partitioning behavior between olivine and silicate melt. *Contrib. Mineral. Petrol.* **172**, 15 (2017).
67. Dalou, C., Koga, K. T., Le Voyer, M. & Shimizu, N. Contrasting partition behavior of F and Cl during hydrous mantle melting: implications for Cl/F signature in arc magmas. *Prog. Earth Planet. Sci.* **1**, 26 (2014).

Acknowledgements

We thank B. Monteleone and N. Chatterjee for their technical expertise on the Cameca 1280 at the Northeast National Ion Microprobe Facility at WHOI and electron microprobe at MIT, respectively. We thank S. Parman, W. J. Collins and R. Loucks for their comments on previous versions of the manuscript.

Author contributions

B.M.U. conceived the study. B.M.U. and V.L.R. collected and interpreted the data and wrote the manuscript. O.J. and O.M. provided samples, data and geochemical models. B.M.U., V.L.R., M.D.B. and E.J.C. acquired financial support. All authors contributed to editing the manuscript. Funding for this study was supported by the Woods Hole Oceanographic Institution Ocean Venture Fund to B.M.U., NSF awards EAR-P&G #1839128 and EAR-P&G/Geophysics #1855302 to V.L.R. and EAR-18-55430 to M.D.B. and E.J.C. V.L.R. also acknowledges the support from the Visiting Scholar at SCIENCE programme at the University of Copenhagen, Denmark. B.M.U. also acknowledges continued support from NSF OCE Post-doctoral Research Fellow grant (#2126559).

Competing interests

The authors declare no competing interests.

Additional information

Supplementary information The online version contains supplementary material available at https://doi.org/10.1038/s41561-022-00947-w.

Correspondence and requests for materials should be addressed to B. M. Urann.

Peer review information *Nature Geoscience* thanks Stephen Parman, William Collins and Robert Loucks for their contribution to the peer review of this work. Primary Handling Editor: Rebecca Neely, in collaboration with the *Nature Geoscience* team.

Reprints and permissions information is available at www.nature.com/reprints.